nanomaterials

MDPI

Article

In Situ Transformed CoOOH@Co_3S_4 Heterostructured Catalyst for Highly Efficient Catalytic OER Application

Abu Talha Aqueel Ahmed [1], Vijaya Gopalan Sree [2], Abhishek Meena [1], Akbar I. Inamdar [1], Hyunsik Im [1] and Sangeun Cho [1,*]

[1] Division of System Semiconductor, Dongguk University, Seoul 04620, Republic of Korea; abutalha.aa@dongguk.edu (A.T.A.A.); abhishek@dongguk.edu (A.M.); akbarphysics@dongguk.edu (A.I.I.)
[2] Department of Physics, Dongguk University, Seoul 04620, Republic of Korea; sreevg@dongguk.edu
* Correspondence: sangeun.c@dongguk.edu; Tel.: +82-2-2260-3770

Abstract: The deprived electrochemical kinetics of the oxygen evolution reaction (OER) catalyst is the prime bottleneck and remains the major obstacle in the water electrolysis processes. Herein, a facile hydrothermal technique was implemented to form a freestanding polyhedron-like Co_3O_4 on the microporous architecture of Ni foam, its reaction kinetics enhanced through sulfide counterpart transformation in the presence of Na_2S, and their catalytic OER performances comparatively investigated in 1 M KOH medium. The formed Co_3S_4 catalyst shows outstanding catalytic OER activity at a current density of 100 mA cm^{-2} by achieving a relatively low overpotential of 292 mV compared to the pure Co_3O_4 catalyst and the commercial IrO_2 catalyst. This enhancement results from the improved active centers and conductivity, which boost the intrinsic reaction kinetics. Further, the optimized Co_3S_4 catalyst exhibits admirable prolonged durability up to 72 h at varied current rates with insignificant selectivity decay. The energy dispersive X-ray spectroscopy (EDX) and Raman spectra measured after the prolonged OER stability test reveal a partial transformation of the active catalyst into an oxyhydroxide phase (i.e., CoOOH@Co_3S_4), which acts as an active catalyst phase during the electrolysis process.

Keywords: hydrothermal growth; anion exchange; water electrolysis; heterostructure; oxygen evolution reaction

check for updates

Citation: Ahmed, A.T.A.; Sree, V.G.; Meena, A.; Inamdar, A.I.; Im, H.; Cho, S. In Situ Transformed CoOOH@Co_3S_4 Heterostructured Catalyst for Highly Efficient Catalytic OER Application. *Nanomaterials* **2024**, *14*, 1732. https://doi.org/10.3390/nano14211732

Academic Editors: Zhao Ding and Liangjuan Gao

Received: 1 October 2024
Revised: 26 October 2024
Accepted: 28 October 2024
Published: 29 October 2024

1. Introduction

Hydrogen (H_2) has emerged as a highly promising, environmentally friendly energy carrier for a sustainable future in the face of growing environmental challenges and energy shortages [1–3]. Owing to the enormously high energy density of 142 MJ kg^{-1}, H_2 presents enormous potential as a clean energy source to lessen dependency on fossil fuels, which is ~70% of the total energy needed around the world [4–7]. The extensive depletion of fossil fuels has led to numerous harmful environmental impacts, including acid rain, air pollution, and global warming. To address these issues, there is an urgent need for an efficient and durable renewable energy system [8]. Utilizing renewable electricity produced by intermittent energy sources like solar and wind power are of great interest, however, their intermittent nature hinders widespread application. Therefore, H_2 is deemed as a highly efficient and carbon-free energy carrier to fulfill the current energy needs [9–12]. However, long-term sustainability is impossible with conventional industrial H_2 production methods like coal gasification and steam methane reforming, which both greatly increase carbon emissions [13–15]. In this regard, water electrolysis is becoming more and more popular as a sustainable and ecologically friendly method of producing high-purity hydrogen [16–19]. The process is restricted despite its potential due to the anode's slow kinetics of the oxygen evolution reaction (OER), which is mediated by a four-electron transfer mechanism. The overall energy conversion efficiency is hindered by this slow OER, which limits the wider use of water electrolysis for large-scale hydrogen production [20–22].

Despite the remarkable OER performance demonstrated by noble metal catalysts like RuO_2 and IrO_2, their high cost and constrained availability prevent their widespread industrial use [21,23,24]. As a result, the first row *3d* transition metals (TM) have drawn a lot of attention because of their strong catalytic activity and abundance in the search for more accessible and affordable alternatives [25]. Among all *3d* TM, Co_3O_4 have drawn a lot of interest due to their exceptional mechanical, physical, and redox properties, as well as affordability, and therefore, have been studied as non-precious metal catalysts for water electrolysis applications [26–31]. However, the scalable utilization is limited due to their poor overpotential (>400 mV at 10 mA cm^{-2}), which falls short for their practical utilization at a larger current scale [32]. To address these issues, various synthesis strategies have been implemented including morphology tuning (e.g., nanocubes, spheres, rods, etc.), nano shape or size engineering, and combining or compositing Co_3O_4 with other materials (e.g., carbon, graphene, Ag, N, S, etc.) which led to improved material conductivity and enhanced catalytically active sites [33,34]. This is because variation of size or shape from bulk to nano results in enhanced specific surface area, which is in direct relation with the active sites, and the integration of heteroatoms alters the electronic structure of the catalyst materials [17]. The catalytic OER performance of Co_3O_4 catalysts can be enhanced by converting oxide into sulfide counter-phase, which can improve both the conductivity and active sites for efficient water electrolysis [35]. It is because the sulfide transformation stands out as a promising approach due to the unoccupied *3d* orbital and the lone pair electrons in the *3p* orbital of sulfur, which are believed to enhance surface charge through donor/acceptor interaction and boost the catalytic OER activity of the Co_3S_4 [36–38].

Based on the above key consideration, in this work, we report the successful growth of binder-free Co_3O_4 with polyhedron-like morphology on the microporous architecture of Ni foam (NF) through a cost-effective hydrothermal process. This formed electrode film then serves as the template to form the desired Co_3S_4 via simple anion exchange reactions using the Na_2S. The catalytic OER activity of the proposed catalyst was enhanced significantly because the substitution of sulfur in the Co_3O_4 materials can improve flexibility and promote more efficient electron transport within the structure, which results in enhanced electrochemical performance [39]. The optimized polyhedron-like Co_3S_4 catalyst achieves the smaller overpotential (292 mV at 100 mA cm^{-2}) and Tafel slope (132 mV dec^{-1}) compared to the Co_3O_4 (410 mV and 156 mV dec^{-1}) catalyst. Further, Co_3S_4 sustained the smaller overpotential at a diverse current density range (100 to 500 mA cm^{-2}) with a static potential response and sustained prolonged chronopotentiometric stability (72 h) without any significant activity decay. These results position the Co_3S_4 as a strong candidate among non-noble metal catalysts for efficient OER in an alkaline medium (Table S1). Besides, the Co_3S_4 was converted into the CoOOH@Co_3S_4 heterostructure phase upon electrooxidation during the chronopotentiometric test. The viable OER activity is likely attributed to the enhanced electronic conductivity, and the increment in the Co^{3+} active centers upon electrooxidation further contributed to enhancing the efficient electron and ion transport [40].

2. Materials and Methods

2.1. Materials

All the chemical reagents used in this experiment were of analytical grade and purchased from Sigma-Aldrich, St. Louis, MO, USA. C_2H_5NS (≥98%), C_2H_5NS (≥98%), KOH (≥85%), CH_3CH_2OH (ethanol; ≥95%), HCl (37%), and CH_3COCH_3 (≥99.5%) were used as received without any purification. Three-dimensionally (3D) microporous Ni foam with sheet size of 200 mm × 300 mm was purchased from Alantum (Seoul, Republic of Korea).

2.2. Synthesis of Co_3O_4 and Co_3S_4 Electrode Films

The Co_3O_4 electrode film was initially deposited on the 3D porous NF (1 × 5 cm^2) using a hydrothermal process followed by air annealing, and then subsequently, anion exchange procedure was implemented to obtain the desired Co_3S_4 electrode film. In a typical synthesis, $C_6H_5Na_3O_7{\cdot}2H_2O$ (6 mmol) and C_2H_5NS (6 mmol) were dissolved in

50 mL of deionized water. Thereafter, $CoCl_2 \cdot 6H_2O$ (6 mmol) was added to the mixture under vigorous stirring for about 30 min. The masked NF substrate (1 × 1 cm^2) and the formed solution were transferred to the Teflon container of the autoclave. The sealed autoclave assembly was kept in a furnace and the deposition was performed at 150 °C for 6 h. The synthesized electrode film was rinsed with deionized water and ethanol and then annealed to get the porous Co_3O_4 phase. In the second step, an anion exchange process was performed on the Co_3O_4 using Na_2S (0.1 M) at 120 °C for 10 h to obtain the Co_3S_4 electrode film.

2.3. Material Characterization

The formed Co_3O_4 and Co_3S_4 electrode films were characterized by the X-ray diffraction (XRD) measurement technique, which was used to analyze the crystallinity and material structure. The XRD spectra were obtained using a Rigaku Smartlab instrument (Tokyo, Japan) at the spectral angle (2θ) range between 20 and 80° with a scanning speed of 2° min^{-1}. The Raman spectroscopy was implemented to investigate the material fingerprints and elemental bonds using a LabRam Aramis instrument (Jobin Yvon, Longjumeau, France). Field emission scanning electron microscope (FE-SEM) coupled with the energy dispersive X-ray spectroscopy (EDX) was employed to evaluate the surface morphology and composition using the JSM-6701F instrument (JEOL, Tokyo, Japan). X-ray photoelectron spectroscopy (XPS) was used to determine the oxidation states of the Co, O, and S constituent elements using a ULVAC PHI 5000 VersaProbe instrument (Kanagawa, Japan), and their respective binding energies were calibrated with the help of carbon (C 1s at 284.30 eV) contaminant as a reference present inside the chamber.

2.4. Catalytic OER Testing

A VersaSTAT instrument (Ametek Scientific Instruments, Berwyn, PA, USA) in the standard three-electrode configuration was used to perform all electrochemical OER testing, which includes linear-sweep voltammetry (LSV), non-Faradaic cyclic voltammetry (CV), chronopotentiometry, and electrochemical impedance spectroscopy (EIS) curves. The electrochemical cell was fabricated using a saturated calomel electrode (SCE; reference electrode), graphite rod (counter electrode), synthesized electrode films (working electrode), and 1.0 M KOH solution (electrolyte). To examine the overpotential (η) response, LSV curves were recorded in a potential window range between 0.0 and 1.0 V (vs. SCE) and the electrolyte solution was continuously stirred during the OER testing. The obtained potentials were converted into a reversible hydrogen electrode (RHE) reference scale and then *JR* compensation was performed to rectify the ohmic losses caused by internal and electrolyte resistance (*Rs*) as follows [41]:

$$E_{RHE} = E_{SCE} + (pH \times 0.059) + E^{\circ}{}_{SCE}, \quad (1)$$

$$E_{RHE}\ (JR \text{ compensated}) = E_{RHE} - (J \times Rs), \quad (2)$$

$$\eta = E_{RHE}\ (JR \text{ compensated}) - 1.23, \quad (3)$$

where E_{RHE} represents the converted potential RHE reference scale, E_{SCE} stands for the obtained potential in the SCE scale, and $E^{\circ}{}_{SCE}$ denotes the standard potential of the SCE electrode at room temperature. The non-Faradaic CV curves were recorded in the potential window range between 0.01 and 0.11 V (vs. SCE) as a function of scan rate to estimate the electrochemical double-layer capacitance (C_{DL}) and electrochemically active surface area (*ECSA*). The electrochemical impedance spectroscopy (EIS) curves were recorded to examine the charge transfer behavior. The EIS curves were measured at a biasing potential of 0.5 V in the broad frequency range between 0.1 and 10 kHz with an AC signal amplitude of 10 mV.

3. Results and Discussion

3.1. Crystallographic Characteristics

Figure 1a shows the schematic representation of the formation of Co_3S_4 from Co_3O_4 involving an anion exchange reaction, where sulfur anions (S^{2-}) replace the oxygen anions (O^{2-}) in Co_3O_4. The composition and crystalline structure of the films were first determined using the XRD technique. As shown in Figure 1b, the displayed XRD patterns of the synthesized films (Co_3O_4 and Co_3S_4) exhibit distinct diffraction peaks, indicating both samples possess good crystallinity. The characteristic peaks of Co_3O_4 (JCPDS card No. 76-1802) at 31.18, 36.64, 38.30, 44.54, 55.30, 73.96, and 77.18 are consistent with the peaks corresponding to the crystal plane of (220), (311), (222), (400), (422), (620), and (533), respectively [42]. After the anion exchange reaction, the diffraction peaks of the obtained sample corresponding to the cubic Co_3S_4 phase (JCPDS card No. 76-1802) can be distinguished in the XRD graph (Figure 1b). Noticeably, the diffraction peaks at 31.24, 37.92, 49.88, 54.94, 75.54, and 78.10 associated with reflections from (311), (400), (511), (440), (642), and (553) planes. This shows that we have successfully synthesized cubic-Co_3S_4 from Co_3O_4 and are also in agreement with the standard JCPDS (card No. 73-1703) data with space group: Fd3-m (227) [43]. To further unveil the formation of Co_3S_4 from Co_3O_4, we conducted ex situ Raman experiments for both Co_3O_4 and Co_3S_4 and their spectra are shown in Figure 1c. Spectra Co_3O_4 samples display five characteristic Raman peaks corresponding to the F_{2g}^1 (~194 cm^{-1}), E_g (~491 cm^{-1}), F_{2g}^2 (~525 cm^{-1}), F_{2g}^3 (~620 cm^{-1}), and A_{1g} (~694 cm^{-1}) phonon modes [44]. Following the formation of cubic Co_3S_4 from Co_3O_4 through the anion exchange reaction, four significantly changed Raman peak signals were observed in the spectra, as shown in Figure 1c. The observed four phonon modes of Co_3S_4 were F_{2g}^1 (~154 cm^{-1}), E_g (~240 cm^{-1}), F_{2g}^3 (~340 cm^{-1}), and A_{1g} (~389 cm^{-1}).

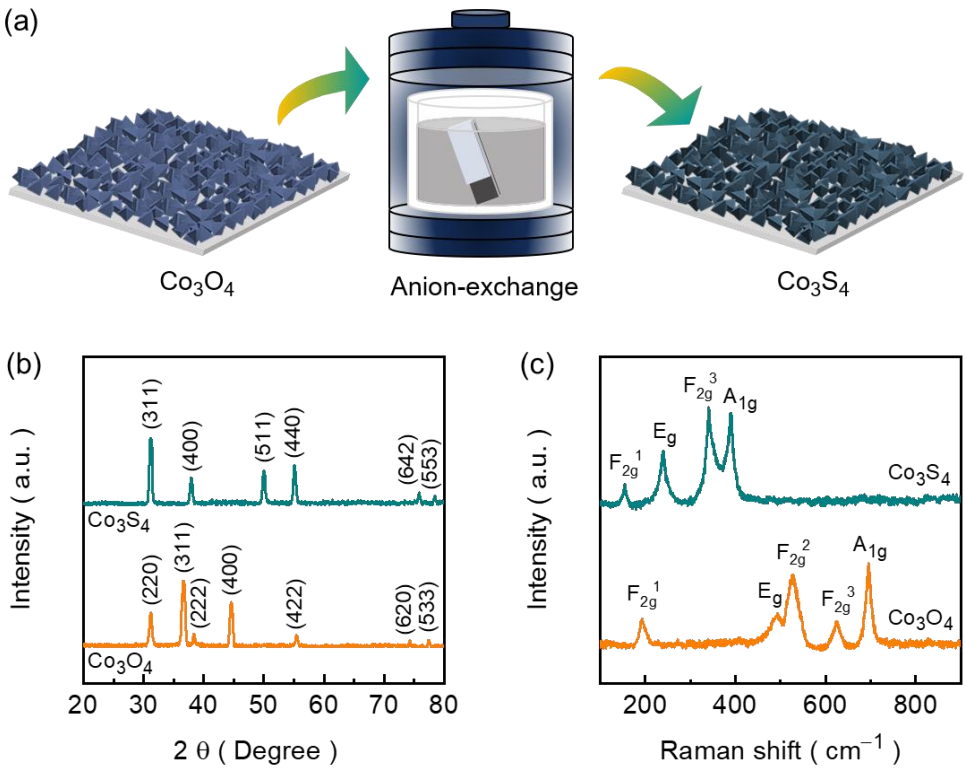

Figure 1. (**a**) Schematic diagram representing the process for the fabrication of Co_3S_4 from Co_3O_4 through anion exchange procedure. Comparative (**b**) XRD and (**c**) Raman spectra of the prepared Co_3S_4 and Co_3O_4 electrode films.

3.2. Morphological and Compositional Properties

The morphologies, microstructures, and elemental distribution of the materials at microstructural levels of Co_3O_4 and Co_3S_4 were analyzed by FE-SEM and FE-SEM-EDX mapping. Figure 2 presents the FE-SEM images of the Co_3O_4 and Co_3S_4 films. The Co_3O_4 electrode film exhibits a polyhedron-like 3D architecture that is randomly stacked and is vertically grown on the pre-cleaned substrate (NF), leading to voids surrounding the irregularly grown polyhedrons during the hydrothermal process, whereas variations of polyhedron size and rougher surface were noted for Co_3S_4 films. This change from a smoother surface of Co_3O_4 to a much rougher surface for Co_3S_4 might be the result of a significant change in the size of polyhedrons during recrystallization during the anion exchange process. Furthermore, SEM-EDX was utilized to analyze the elemental composition and distribution of materials at microstructural levels. Figure S1 shows the obtained EDX spectra of Co_3O_4 and Co_3S_4 electrode films, and their extracted chemical composition and distribution summed up in the inset of Figure S1, revealing the stoichiometric chemical compositions of the respective electrode film.

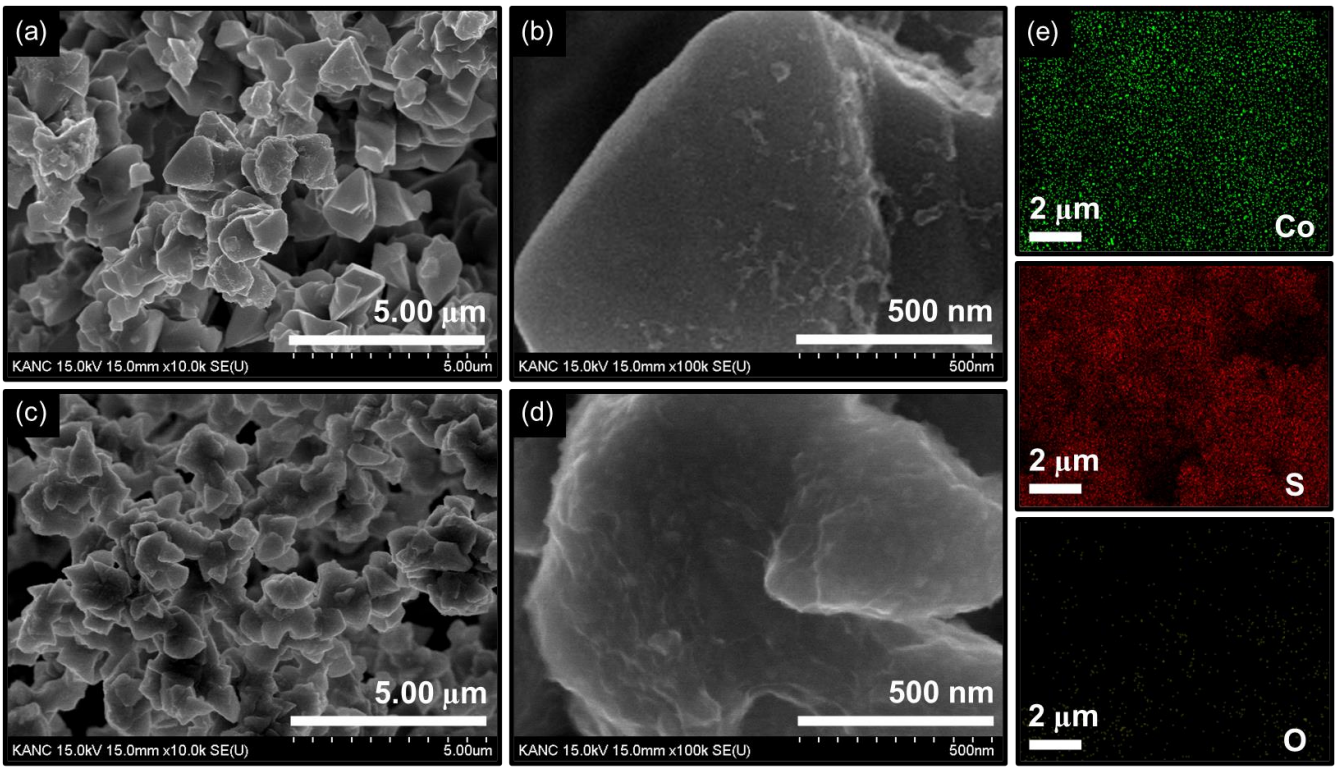

Figure 2. Low and high magnifications FE-SEM images of (**a**,**b**) Co_3O_4 and (**c**,**d**) Co_3S_4 electrode films. (**e**) FE-SEM-EDX mapping images for the transformed Co_3S_4 electrode films.

3.3. Chemical State Characteristics

For the detailed investigation of surface chemistry, XPS was further employed to analyze the elemental composition, chemical states, and electronic structure of Co_3O_4 and Co_3S_4 electrode films. All of the obtained core-level XPS emission spectra were best fitted using the Gaussian curve fitting model to reconstruct the XPS spectra. Figure 3a shows the survey spectra of Co_3O_4 and Co_3S_4 electrode films. The Co_3O_4 spectra show three peaks located at 284.30, 531.07, and 779.69 eV, corresponding to the C 1s, O 1s, and Co 2p degenerate states. However, after the phase transformation, an additional emission peak related to S 2p was observed at 162.84 eV. The additional C 1s peak apart from the constituent elements' emission aroused from the contaminated carbon present inside the vacuum chamber. Figure 3c shows the Co 2p core-level spectra for Co_3O_4 and Co_3S_4 electrode films, which display a total of four emission peaks where the two most intense

peaks of four are deconvoluted into doublets. These six emission peaks of Co_3O_4 were located at 778.78, 781.27, 787.46 (satellite [Sat.]), 794.51, 796.90, and 803.83 (Sat.) eV. The higher and lower energy peaks correspond to Co $2p_3/_2$ and Co $2p_1/_2$, respectively. The energy separation of 15.73 eV between Co $2p_1/_2$ and Co $2p_3/_2$ confirms a mixed Co^{3+} and Co^{2+} oxidation state present in the Co_3O_4 structure [30,45]. Figure 3d shows the O 1s spectrum of Co_3O_4, which shows two superimposed peaks deconvoluted into three. The first peak present at 529.47 eV represents lattice oxygen (O_1), the second peak positioned at 531.49 eV originated from the oxygen vacancies (O_2), and the third peak located at 532.95 eV corresponds to chemisorbed/dissociated oxygen species (O_3) [46]. As shown in Figure 3e, following the anion exchange, the formation of the new S 2p signal appears for the Co_3S_4 film while the previous O 1s peaks diminish and nearly vanish. Two characteristic peaks were observed at 162.74 (S $2p_{3/2}$) and 163.93 (S $2p_{1/2}$) eV, respectively. The 1.19 eV energy difference between S $2p_1/_2$ and S $2p_3/_2$ indicates the presence of divalent sulfur (S^{2-}) bonded to Co^{2+} and Co^{3+} in Co_3S_4 [47]. The weak O 1s peaks suggest partial surface oxidation, which might arise due to air oxidation on the surface during sample preparation. The separation energy between Co $2p_1/_2$ and Co $2p_3/_2$ in Co_3S_4 remains almost consistent with that in Co_3O_4. Thus, the formation of pure Co_3O_4 and its subsequent conversion into Co_3S_4 is confirmed using XPS analysis.

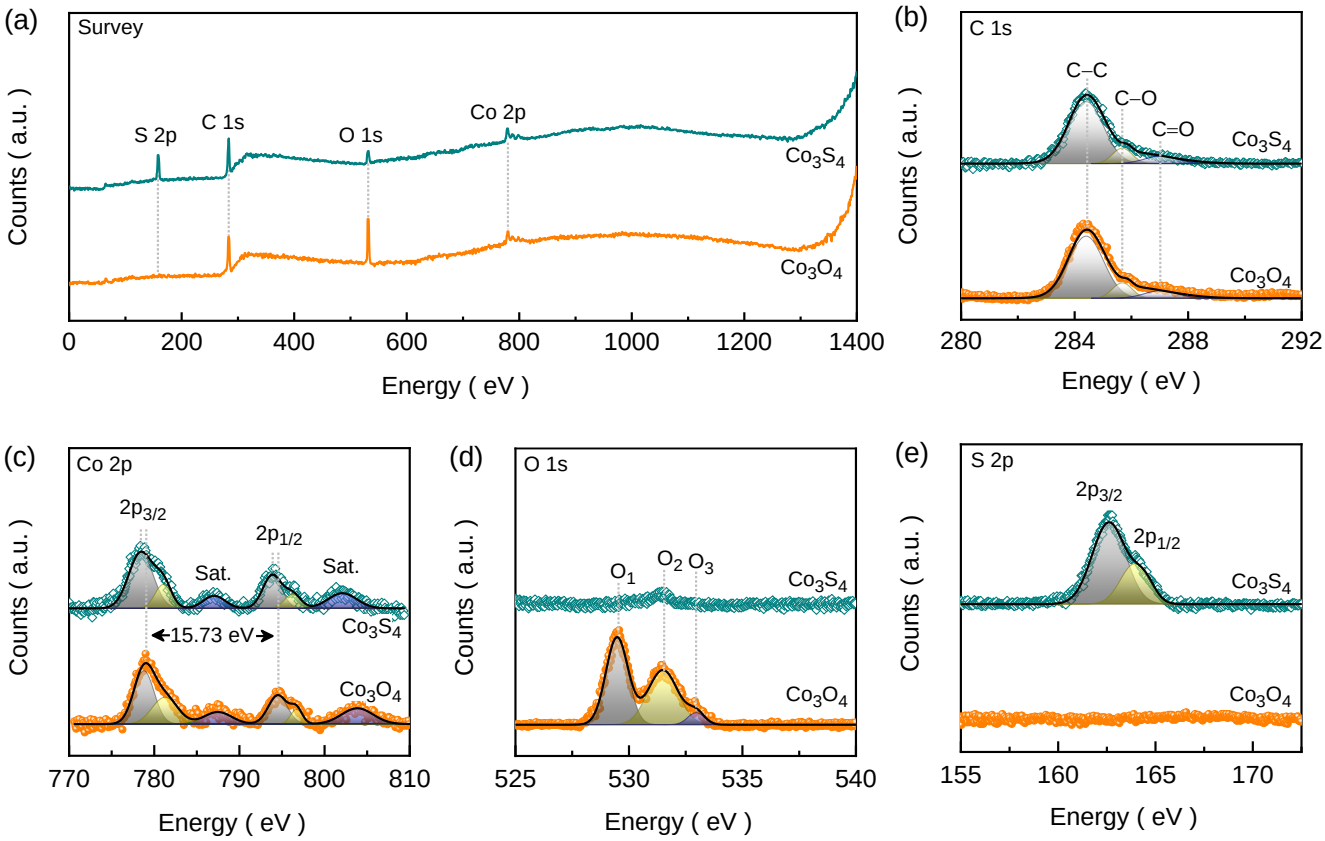

Figure 3. (**a**) High-resolution XPS survey spectra and the narrow-ranged XPS emission spectra for (**b**) C 1s (**c**) Co 2p, (**d**) O 1s, and (**e**) S 2p of the Co_3O_4 and Co_3S_4 electrode films. The high-resolution emission spectra were deconvoluted using the Gaussian curve fitting model.

3.4. Electrocatalytic OER Performances

The catalytic performance of the formed polyhedron-like Co_3O_4 and Co_3S_4 catalyst films were evaluated using the LSV curves, which reveals the significant variation in the redox properties and the catalytic OER performances after the substitution of sulfide ions in the oxide cocatalyst material. For comparison, the control catalysts including a commercial IrO_2 benchmark supported on NF substrate as well as bare NF substrate were also examined

at the same experimental condition. The selection of reference catalysts provides a thorough basis for evaluating the catalytic OER performance of the proposed materials, with IrO_2 serving as a high-activity standard and the bare NF offering a baseline to understand the contributions of the constituent components to the overall catalytic behavior. Figure 4a shows the typical *JR* compensated OER LSV curves for the Co_3O_4, Co_3S_4, NF substrate, and IrO_2 catalyst films recorded in an alkaline KOH solution (1.0 M) medium. The LSV curve of the bare NF substrate exhibited a very low OER current response throughout the potential sweep compared to the formed catalysts, suggesting that the NF substrate itself was not electrochemically active. Interestingly, the polyhedron-like Co_3S_4 catalyst exhibited superior electrocatalytic activity compared to the other catalyst films, achieving a high current density of 100 mA cm^{-2} at a small overpotential of 292 mV (vs. RHE). Evidently, this overpotential value is lower than the pure Co_3O_4 (410 mV vs. RHE) catalyst and NF substrate (708 mV vs. RHE), and even surpasses the catalytic activity of the IrO_2 (362 mV vs. RHE) catalysts at the same current density.

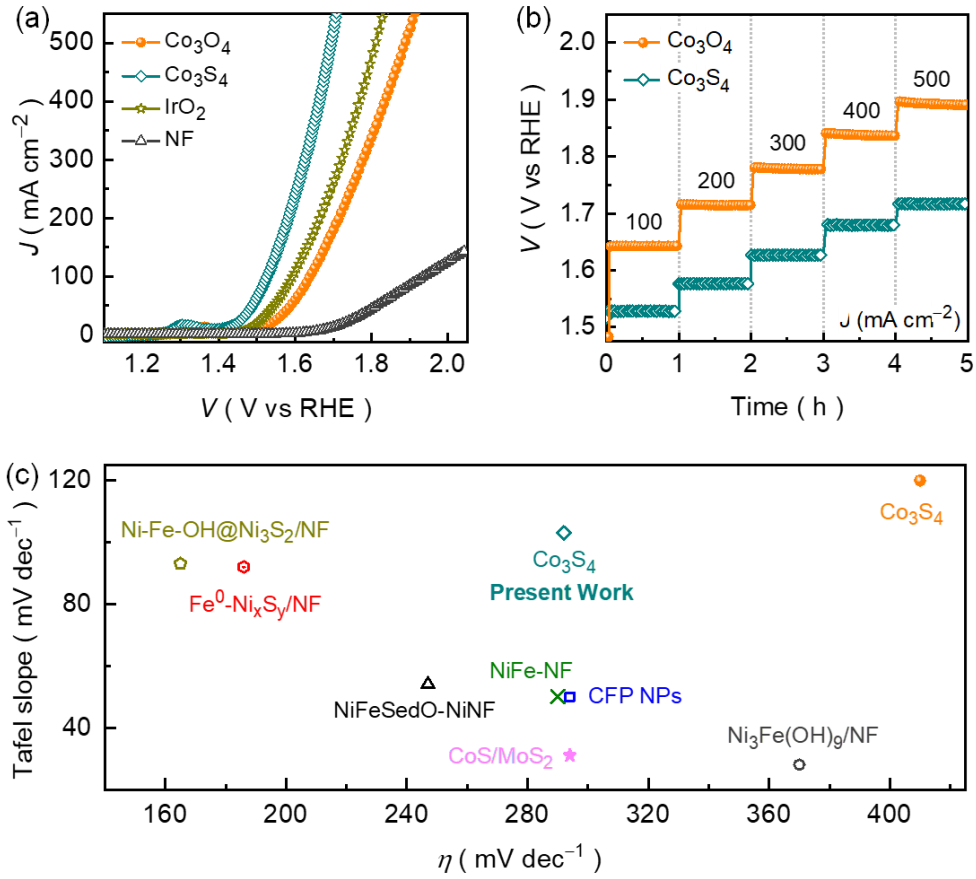

Figure 4. (**a**) LSV curves and (**b**) voltage-step profile for the Co_3O_4 and Co_3S_4 catalyst films. (**c**) Comparative electrocatalytic OER performance of various cobalt-based catalysts with the proposed polyhedron-like Co_3S_4 catalyst measured at a current density of 100 mA cm^{-2}.

Moreover, the overpotentials required to drive the current densities of 200, 300, 400, and 500 mA cm^{-2} for the polyhedron-like Co_3S_4 catalyst were 352, 395, 431, and 463 mV, respectively. However, to drive the same anodic current densities, the required overpotentials for the Co_3O_4 catalyst were 483, 546, 604, and 657 mV (vs. RHE). The smaller overpotentials of the Co_3S_4 catalyst at all anodic current densities demonstrated its superior catalytic OER activity compared to that of the pure Co_3O_4 catalyst. The noticeable improvement in the catalytic activity of the Co_3S_4 catalyst suggests that the substitution of sulfur with oxygen constituent enhances the material conductivity (Figure S2) and elevates the accessible active sites (Figure S3), thereby improving electron transfer throughout the polyhedron

network [48–50]. This increased electron mobility leads to faster reaction kinetics, as the sulfur atoms modify the electronic properties, lowering energy barriers, and facilitating more efficient catalytic reactions [51–53].

The overpotentials of the Co_3O_4 and Co_3S_4 catalysts at various current densities can also be assessed from their respective chronopotentiometric rate performance curves. Figure 4b shows the chronopotentiometric voltage-step profile curve being the function of current density. The applied current density rate was constantly maintained for an hour at 100 mA cm^{-2} and then gradually increased up to 500 mA cm^{-2} with an interval of 100 mA cm^{-2} to highlight the potential response at varied current rates. Both electrocatalysts exhibit static potential response throughout the voltage-step profile and demonstrate the direct relationship between the potential and applied current density. Clearly, the Co_3S_4 catalyst achieved a smaller potential response at each voltage step compared to the pure Co_3O_4 catalyst, which is a result of efficient mass transport with improved conductivity (Table 1). These results are further supported by the *ECSA*-compensated LSV curve (Figure S4a), which reveals the Co_3S_4 catalyst consistently maintains a lower potential response at each driven *ECSA*-compensated current density (J_{ECSA}), further confirming the superior catalytic OER performance of Co_3S_4 than Co_3S_4 catalyst. Besides, the Co_3S_4 catalyst demonstrated the competitive catalytic OER activity compared to the other noble metal-free catalysts in an alkaline KOH medium (Figure 4c and Table S1).

Table 1. The EIS curves fitted parameter values obtained using Z-view software (serial #13339, Scribner Associates, Inc., Southern Pines, NC, USA) for the pure Co_3O_4 and Co_3S_4 catalysts (*Rct*; change in charge transfer resistance).

Electrocatalyst	Before Catalytic OER Stability		After Catalytic OER Stability	
	Rs (Ω)	*Rct* (Ω)	*Rs* (Ω)	*Rct* (Ω)
Co_3O_4	0.435	7.29	-	-
Co_3S_4	0.386	4.48	0.401	4.72

The variation in the overpotential is directly associated with the enhanced reaction kinetics, which can be better understood by examining the Tafel curves. The steepness of the Tafel curve provides insight into the reaction rate kinetics and the efficiency of the catalyst. Figure 4b presents the Tafel plots derived from the chronopotentiometric curves using the Tafel equation:

$$\eta = \alpha + [\log (J) \times \beta], \quad (4)$$

where α, J, and β represent the constant of the equation, current density, and the Tafel slope, respectively. A comparatively small Tafel slope of 132 mV dec^{-1} was estimated for the Co_3S_4 catalyst compared to the pure Co_3O_4 (156 mV dec^{-1}) catalyst, highlighting the superior catalytic efficiency and rapid OER kinetics of the catalyst electrode after the anion exchange process. The distinct reduction in the Tafel slope was aroused due to the enhanced material conductivity and simultaneously increased a larger number of catalytically active sites which are associated with the substitution of sulfur by oxygen, resulting in the enhanced catalytic OER reaction kinetics. Notably, the catalytic OER performances of the Co_3S_4 catalyst were found to be highly reliable, as demonstrated in the sequential independent tests (Figure 5b). Moreover, the intrinsic OER reaction kinetics of the catalyst material is also closely related to their respective turnover frequency (TOF), which further quantifies the efficiency of the catalyst by measuring the number of molecules that react at the available electrocatalytically active sites per unit of time and can be calculated using the following equation:

$$TOF = [J \times A]/[n \times F \times N], \quad (5)$$

where "n" stands for the number of moles of the active electrocatalyst, which can be determined based on the loading weight and molecular weight of the active catalyst material deposited on the NF substrate. The value of n is 8.31 and 6.56 $\times$ 10^{-6} moles for Co_3O_4 and Co_3S_4, respectively. The factor "N (for OER it is 4)" accounts for the four

electrons involved per mole of oxygen in the reaction. "*A*" and "*F*" denote the active catalyst deposition area (cm^2) and the Faraday constant (96,485.3329 A·s mol^{-1}). Figure S3a shows the *TOF* curves for the Co_3O_4 and Co_3S_4 catalysts obtained from the measured LSV curves. A significantly higher *TOF* of 0.2826 s^{-1} was calculated for the Co_3S_4 catalyst at 1.739 V (vs. RHE) compared to the Co_3O_4 catalyst (0.0739 s^{-1}). This enhancement is approximately four-fold greater than the pristine catalyst at the same driving potential, indicating that the sulfur substitution effectively enhances the reaction kinetics by promoting more efficient electron and ion transport throughout the catalyst network.

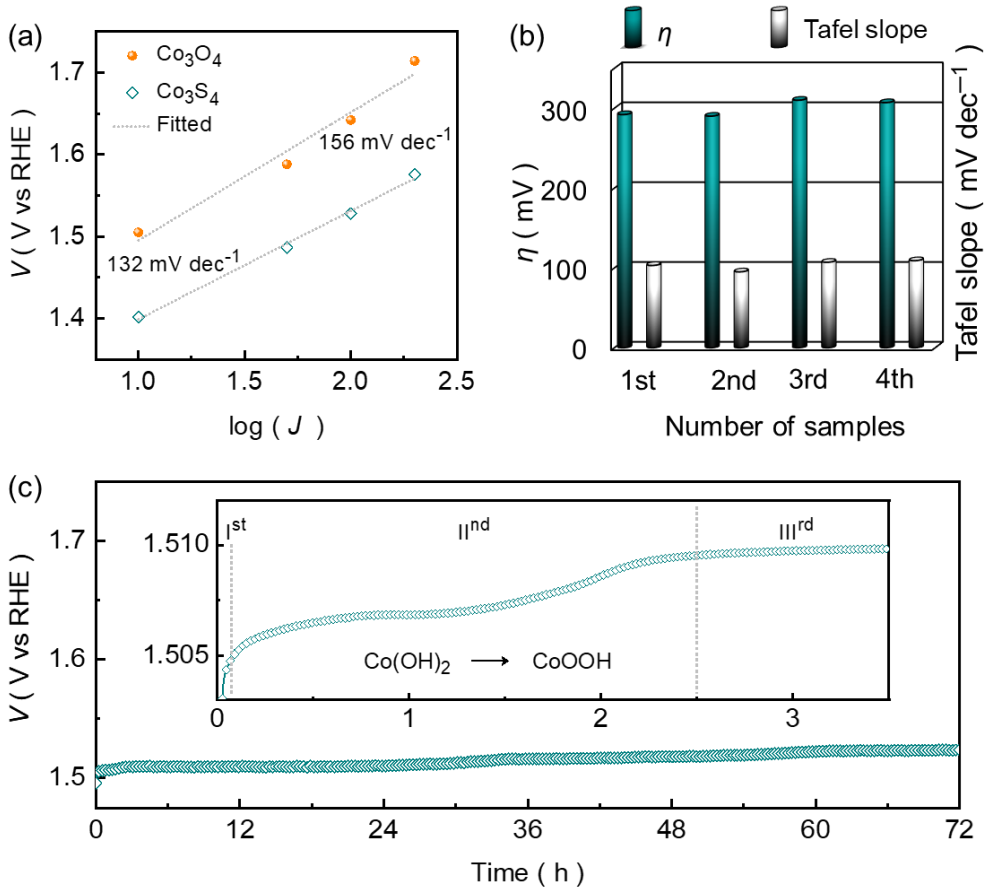

Figure 5. (**a**) Tafel slope for the Co_3O_4 catalyst films. (**b**) Reliability of the Co_3S_4 for the catalytic OER. (**c**) Prolonged chronopotentiometric OER stability of Co_3S_4 catalyst measured up to 72 h at a current density of 100 mA cm^{-2}.

Apart from the catalytic ascendency of the Co_3S_4 for OER, the long-term durability in alkaline medium is the characteristic feature of an efficient catalyst for their practical utilization. Figure 5c shows the prolonged chronopotentiometric stability performance of the polyhedron-like Co_3S_4 catalyst toward the OER in an alkaline KOH medium. The chronopotentiometric stability curve was recorded at an applied current density of 100 mA cm^{-2} with continuous electrolysis for up to 72 h. The Co_3S_4 catalyst exhibited quite a stable voltage response during the vigorous and continuous gas bubble evolution at a high current density of 100 mA cm^{-2}, which is attributed to efficient electron and ion transport demonstrating the strong durability during the prolonged catalytic OER test. This analysis is further supported by the EIS curve (Figure S4c), which shows the insignificant change in charge transfer resistance after the prolonged catalytic OER testing. Moreover, an almost identical LSV curve (Figure S4d) further confirmed its exceptional long-term OER performance in an alkaline environment.

Conspicuously, the chronopotentiometric curve reveals the small potential loss at the beginning of the test, which is shown in the inset of Figure 5c. This dramatic change

in the potential is associated with the in situ partial phase transformation of an active Co_3S_4 catalyst into CoOOH at the surface upon electrooxidation process forming the CoOOH@Co_3S_4 heterostructure, which serves as the active catalytic center and is typical for Co-based catalyst during the OER process [54]. This phase transformation can be quantitively understood from the three distinct potential regions (inset of Figure 5c). To gain further insight into the phase transformation during the catalytic OER process, the ex-situ EDX (Figure S5a), Raman (Figure S5b), and the narrow XPS (Figure S6) spectra were recorded after the prolonged chronopotentiometric stability to understand the changes in the chemical composition and chemical bonds of the catalyst. The EDX spectrum revealed the sulfur deficiency in the constituent composition with an abrupt rise in the oxygen percentage, which is obvious during the OER in an alkaline medium. This analysis is consistent with the post-stability measured XPS emission spectra, which further revealed the decreased S 2p peak (Figure S6b) intensity caused due to the depletion of sulfur and the simultaneously increased O 1s peak (Figure S6c) intensity upon electrooxidation process in an alkaline KOH medium [40]. Besides, the spin-energy separation of Co $2p_3/_2$ and Co $2p_1/_2$ (Figure S6a) degenerate state reduced to 15.31 eV, indicating the partial alteration of Co^{2+} into Co^{3+} during the chronopotentiometric stability, as illustrated in the inset of Figure 5c. Further, the Raman spectrum reveals an additional peak positioned at ~505 cm^{-1}, originated due to the presence of CoOOH species, validating the catalyst phase transformation during the catalytic OER process.

4. Conclusions

The polyhedron-like Co_3S_4 phase was transformed successfully via an anion exchange process of the Co_3O_4 template using Na_2S, which was synthesized through a cost-effective and eco-friendly hydrothermal process followed by calcination in ambient air. The polyhedral Co_3S_4 structure served as the highly efficient OER catalyst in an alkaline electrolyte environment. A comprehensive electrocatalytic OER study concludes that the synergistic contribution from the multivalence cobalt state, 3D polyhedral structure, and improved material conductivity support plays a crucial role in enhancing catalytic kinetics, primarily by providing better active site accessibility, *TOF*, and improved electron transport. The optimized Co_3S_4 catalyst demonstrated excellent catalytic OER activity in alkaline 1.0 M KOH condition by achieving a significantly reduced overpotential of 292 mV at a high current density of 100 mA cm^{-2} with the small Tafel slope of 132 mV dec^{-1} compared to the pure Co_3O_4 (410 mV and 156 mV dec^{-1}) catalyst along with the higher normalized J_{ECSA} values at each potential. Further, the Co_3S_4 catalyst maintains the static potential response between the current density rate of 100 and 500 mA cm^{-2} and reveals excellent prolonged endurance up to 72 h at 100 mA cm^{-2}. A notable phase transformation of an active Co_3S_4 catalyst into CoOOH@Co_3S_4 was observed after the chronopotentiometric stability test, which was affirmed through the post-stability measured EDX, Raman, and XPS spectra.

Supplementary Materials: The following supporting information can be downloaded at: https://www.mdpi.com/article/10.3390/nano14211732/s1, Figure S1: EDX spectra; Figure S2: EIS curves; Figure S3: Non-Faradaic CV curves for the estimation of *ECSA*; Figure S4: *ECSA*-compensated LSV curves, TOF curves, and post-stability recorded LSV and EIS curves; Figure S5: post-stability recorded EDX and Raman spectra; Figure S6: post-stability recorded XPS spectra. Table S1: The electrocatalytic OER performance of our optimized Co_3S_4 catalyst films and other metal sulfide-based catalyst in alkaline electrolyte medium at 100 mA cm^{-2} [55–62].

Author Contributions: Conceptualization, methodology, investigation, and writing—original draft preparation, A.T.A.A.; writing, validation, V.G.S.; software, visualization, A.M.; formal analysis, software, data curation, A.I.I.; resources, project administration, H.I.; supervision, writing—review and editing, S.C. All authors have read and agreed to the published version of the manuscript.

Funding: This research was funded by the National Research Foundation of Korea under the Basic Science Research Program (Grant number: RS-2023-00236798).

Data Availability Statement: The data presented in this study are available on reasonable request from the corresponding author.

Conflicts of Interest: The authors declare that they have no conflicts of interest.

References

1. Zhao, Z.; Liu, H.; Gao, W.; Xue, W.; Liu, Z.; Huang, J.; Pan, X.; Huang, Y. Surface-Engineered PtNi-O Nanostructure with Record-High Performance for Electrocatalytic Hydrogen Evolution Reaction. *J. Am. Chem. Soc.* **2018**, *140*, 9046–9050. [CrossRef] [PubMed]
2. Jiao, Y.; Zheng, Y.; Jaroniec, M.; Qiao, S.Z. Design of electrocatalysts for oxygen- and hydrogen-involving energy conversion reactions. *Chem. Soc. Rev.* **2015**, *44*, 2060–2086.
3. Jin, H.; Guo, C.; Liu, X.; Liu, J.; Vasileff, A.; Jiao, Y.; Zheng, Y.; Qiao, S.-Z. Emerging Two-Dimensional Nanomaterials for Electrocatalysis. *Chem. Rev.* **2018**, *118*, 6337–6408. [CrossRef]
4. Chen, J.G.; Crooks, R.M.; Seefeldt, L.C.; Bren, K.L.; Bullock, R.M.; Darensbourg, M.Y.; Holland, P.L.; Hoffman, B.; Janik, M.J.; Jones, A.K.; et al. Beyond fossil fuel–driven nitrogen transformations. *Science* **2018**, *360*, eaar6611. [CrossRef] [PubMed]
5. Hassan, Q.; Algburi, S.; Sameen, A.Z.; Salman, H.M.; Jaszczur, M. Green hydrogen: A pathway to a sustainable energy future. *Int. J. Hydrogen Energy* **2024**, *50*, 310–333. [CrossRef]
6. Zhang, X.; Jia, F.; Song, S. Recent advances in structural engineering of molybdenum disulfide for electrocatalytic hydrogen evolution reaction. *Chem. Eng. J.* **2021**, *405*, 127013. [CrossRef]
7. Yu, J.; Li, Z.; Liu, T.; Zhao, S.; Guan, D.; Chen, D.; Shao, Z.; Ni, M. Morphology control and electronic tailoring of CoxAy (A = P, S, Se) electrocatalysts for water splitting. *Chem. Eng. J.* **2023**, *460*, 141674. [CrossRef]
8. Song, J.; Wei, C.; Huang, Z.-F.; Liu, C.; Zeng, L.; Wang, X.; Xu, Z.J. A review on fundamentals for designing oxygen evolution electrocatalysts. *Chem. Soc. Rev.* **2020**, *49*, 2196–2214. [CrossRef]
9. Tang, C.; Zheng, Y.; Jaroniec, M.; Qiao, S.-Z. Electrocatalytic Refinery for Sustainable Production of Fuels and Chemicals. *Angew. Chem. Int. Ed.* **2021**, *60*, 19572–19590. [CrossRef]
10. Ikuerowo, T.; Bade, S.O.; Akinmoladun, A.; Oni, B.A. The integration of wind and solar power to water electrolyzer for green hydrogen production. *Int. J. Hydrogen Energy* **2024**, *76*, 75–96. [CrossRef]
11. Aslam, S.; Rani, S.; Lal, K.; Fatima, M.; Hardwick, T.; Shirinfar, B.; Ahmed, N. Electrochemical hydrogen production: Sustainable hydrogen economy. *Green Chem.* **2023**, *25*, 9543–9573. [CrossRef]
12. Marouani, I.; Guesmi, T.; Alshammari, B.M.; Alqunun, K.; Alzamil, A.; Alturki, M.; Hadj Abdallah, H. Integration of Renewable-Energy-Based Green Hydrogen into the Energy Future. *Processes* **2023**, *11*, 2685. [CrossRef]
13. Yuan, C.-Z.; Hui, K.S.; Yin, H.; Zhu, S.; Zhang, J.; Wu, X.-L.; Hong, X.; Zhou, W.; Fan, X.; Bin, F.; et al. Regulating Intrinsic Electronic Structures of Transition-Metal-Based Catalysts and the Potential Applications for Electrocatalytic Water Splitting. *ACS Mater. Lett.* **2021**, *3*, 752–780. [CrossRef]
14. Anam, M.; Gomes, H.I.; Rivers, G.; Gomes, R.L.; Wildman, R. Evaluation of photoanode materials used in biophotovoltaic systems for renewable energy generation. *Sustain. Energy Fuels* **2021**, *5*, 4209–4232. [CrossRef]
15. Islam, M.H.; Burheim, O.S.; Pollet, B.G. Sonochemical and sonoelectrochemical production of hydrogen. *Ultrason. Sonochem.* **2019**, *51*, 533–555. [CrossRef]
16. Stamenkovic, V.R.; Strmcnik, D.; Lopes, P.P.; Markovic, N.M. Energy and fuels from electrochemical interfaces. *Nat. Mater.* **2017**, *16*, 57–69. [CrossRef]
17. Aqueel Ahmed, A.T.; Hou, B.; Chavan, H.S.; Jo, Y.; Cho, S.; Kim, J.; Pawar, S.M.; Cha, S.; Inamdar, A.I.; Kim, H.; et al. Self-Assembled Nanostructured $CuCo_2O_4$ for Electrochemical Energy Storage and the Oxygen Evolution Reaction via Morphology Engineering. *Small* **2018**, *14*, 1800742. [CrossRef]
18. Amini Horri, B.; Ozcan, H. Green hydrogen production by water electrolysis: Current status and challenges. *Curr. Opin. Green. Sustain. Chem.* **2024**, *47*, 100932. [CrossRef]
19. Zeng, K.; Zhang, D. Recent progress in alkaline water electrolysis for hydrogen production and applications. *Progress Energy Combust. Sci.* **2010**, *36*, 307–326. [CrossRef]
20. Li, J.; Xie, W.; Zhou, H.; Li, Z.; Shao, M. Techno-economic analysis of electrochemical hydrogen production coupled with alternative oxidation. *Chem. Eng. Sci.* **2024**, *298*, 120322. [CrossRef]
21. Browne, M.P.; Nolan, H.; Duesberg, G.S.; Colavita, P.E.; Lyons, M.E.G. Low-Overpotential High-Activity Mixed Manganese and Ruthenium Oxide Electrocatalysts for Oxygen Evolution Reaction in Alkaline Media. *ACS Catal.* **2016**, *6*, 2408–2415. [CrossRef]
22. Cheng, Y.; Wang, L.; Song, Y.; Zhang, Y. Deep insights into the exfoliation properties of MAX to MXenes and the hydrogen evolution performances of 2D MXenes. *J. Mater. Chem. A* **2019**, *7*, 15862–15870. [CrossRef]
23. Seh, Z.W.; Kibsgaard, J.; Dickens, C.F.; Chorkendorff, I.; Nørskov, J.K.; Jaramillo, T.F. Combining theory and experiment in electrocatalysis: Insights into materials design. *Science* **2017**, *355*, eaad4998. [CrossRef] [PubMed]
24. Oh, H.-S.; Nong, H.N.; Reier, T.; Bergmann, A.; Gliech, M.; Ferreira de Araújo, J.; Willinger, E.; Schlögl, R.; Teschner, D.; Strasser, P. Electrochemical Catalyst–Support Effects and Their Stabilizing Role for IrO_x Nanoparticle Catalysts during the Oxygen Evolution Reaction. *J. Am. Chem. Soc.* **2016**, *138*, 12552–12563. [CrossRef] [PubMed]

25. Yaseen, F.; Hashmi, M.A.; Ain, Q.U.; Lakhani, A.; Ayub, K. The first row transition metal-corrole complexes as a single atom catalyst for electrochemical hydrogen evolution reaction: A DFT insight. *Int. J. Hydrogen Energy* **2024**, *57*, 1389–1397. [CrossRef]
26. Mugheri, A.Q.; Otho, A.A.; Mugheri, A.A. Meritorious spatially on hierarchically Co_3O_4/MoS_2 phase nanocomposite synergistically a high-efficient electrocatalyst for hydrogen evolution reaction performance: Recent advances & future perspectives. *Int. J. Hydrogen Energy* **2021**, *46*, 22707–22718. [CrossRef]
27. Zhao, M.; Liang, H. Crystal Facet Regulation and Ru Incorporation of Co_3O_4 for Acidic Oxygen Evolution Reaction Electrocatalysis. *ACS Nanosci. Au* **2024**, 1–7. [CrossRef]
28. Blakemore, J.D.; Gray, H.B.; Winkler, J.R.; Müller, A.M. Co_3O_4 Nanoparticle Water-Oxidation Catalysts Made by Pulsed-Laser Ablation in Liquids. *ACS Catal.* **2013**, *3*, 2497–2500. [CrossRef]
29. Wiegmann, T.; Pacheco, I.; Reikowski, F.; Stettner, J.; Qiu, C.; Bouvier, M.; Bertram, M.; Faisal, F.; Brummel, O.; Libuda, J.; et al. Operando Identification of the Reversible Skin Layer on Co_3O_4 as a Three-Dimensional Reaction Zone for Oxygen Evolution. *ACS Catal.* **2022**, *12*, 3256–3268. [CrossRef]
30. Kim, M.G.; Choi, Y.-H. Electrocatalytic Properties of Co_3O_4 Prepared on Carbon Fibers by Thermal Metal–Organic Deposition for the Oxygen Evolution Reaction in Alkaline Water Electrolysis. *Nanomaterials* **2023**, *13*, 1021. [CrossRef]
31. Hu, C.; Sun, D.; Liu, J.; Zhang, Q.; Li, X.; Fu, H.; Liu, M.; Xu, J.; Jiang, G.; Lu, Y. Enhanced Electrocatalytic Water Oxidation of Ultrathin Porous Co_3O_4 Nanosheets by Physically Mixing with Au Nanoparticles. *Nanomaterials* **2022**, *12*, 4419. [CrossRef]
32. Zhu, Y.; Wang, J.; Koketsu, T.; Kroschel, M.; Chen, J.-M.; Hsu, S.-Y.; Henkelman, G.; Hu, Z.; Strasser, P.; Ma, J. Iridium single atoms incorporated in Co_3O_4 efficiently catalyze the oxygen evolution in acidic conditions. *Nat. Commun.* **2022**, *13*, 7754. [CrossRef] [PubMed]
33. Amin, H.M.A.; Zan, L.; Baltruschat, H. Boosting the bifunctional catalytic activity of Co_3O_4 on silver and nickel substrates for the alkaline oxygen evolution and reduction reactions. *Surf. Interfaces* **2024**, *54*, 105218. [CrossRef]
34. Liu, Z.; Corva, M.; Amin, H.M.A.; Blanc, N.; Linnemann, J.; Tschulik, K. Single Co_3O_4 Nanocubes Electrocatalyzing the Oxygen Evolution Reaction: Nano-Impact Insights into Intrinsic Activity and Support Effects. *Int. J. Mol. Sci.* **2021**, *22*, 13137. [CrossRef] [PubMed]
35. Aqueel Ahmed, A.T.; Sekar, S.; Lee, S.; Im, H.; Preethi, V.; Ansari, A.S. Nitrogen-doped cobalt sulfide as an efficient electrocatalyst for hydrogen evolution reaction in alkaline and acidic media. *Int. J. Hydrogen Energy* **2022**, *47*, 40340–40348. [CrossRef]
36. Pujari, R.B.; Gund, G.S.; Patil, S.J.; Park, H.S.; Lee, D.-W. Anion-exchange phase control of manganese sulfide for oxygen evolution reaction. *J. Mater. Chem. A* **2020**, *8*, 3901–3909. [CrossRef]
37. Toe, C.Y.; Zheng, Z.; Wu, H.; Scott, J.; Amal, R.; Ng, Y.H. Transformation of Cuprous Oxide into Hollow Copper Sulfide Cubes for Photocatalytic Hydrogen Generation. *J. Phys. Chem. C* **2018**, *122*, 14072–14081. [CrossRef]
38. Li, X.; Ji, M.; Li, H.; Wang, H.; Xu, M.; Rong, H.; Wei, J.; Liu, J.; Liu, J.; Chen, W.; et al. Cation/Anion Exchange Reactions toward the Syntheses of Upgraded Nanostructures: Principles and Applications. *Matter* **2020**, *2*, 554–586. [CrossRef]
39. Duan, J.; Chen, S.; Jaroniec, M.; Qiao, S.Z. Heteroatom-Doped Graphene-Based Materials for Energy-Relevant Electrocatalytic Processes. *ACS Catal.* **2015**, *5*, 5207–5234. [CrossRef]
40. Amin, H.M.A.; Attia, M.; Tetzlaff, D.; Apfel, U.-P. Tailoring the Electrocatalytic Activity of Pentlandite $Fe_xNi_{9-X}S_8$ Nanoparticles via Variation of the Fe : Ni Ratio for Enhanced Water Oxidation. *ChemElectroChem* **2021**, *8*, 3863–3874. [CrossRef]
41. Ahmed, A.T.A.; Ansari, A.S.; Sree, V.G.; Jana, A.; Meena, A.; Sekar, S.; Cho, S.; Kim, H.; Im, H. Nitrogen-Doped CuO@CuS Core–Shell Structure for Highly Efficient Catalytic OER Application. *Nanomaterials* **2023**, *13*, 3160. [CrossRef] [PubMed]
42. Martens, D.L.; Wang, D.K.; Motuzas, J.; Smart, S.; da Costa, J.C.D. Modulation of microporous/mesoporous structures in self-templated cobalt-silica. *Sci. Rep.* **2015**, *5*, 7970. [CrossRef] [PubMed]
43. Zhai, Y.; Mao, H.; Liu, P.; Ren, X.; Xu, L.; Qian, Y. Facile fabrication of hierarchical porous rose-like $NiCo_2O_4$ nanoflake/$MnCo_2O_4$ nanoparticle composites with enhanced electrochemical performance for energy storage. *J. Mater. Chem. A* **2015**, *3*, 16142–16149. [CrossRef]
44. Liu, Z.; Amin, H.M.A.; Peng, Y.; Corva, M.; Pentcheva, R.; Tschulik, K. Facet-Dependent Intrinsic Activity of Single Co_3O_4 Nanoparticles for Oxygen Evolution Reaction. *Adv. Funct. Mater.* **2023**, *33*, 2210945. [CrossRef]
45. Zan, L.; Amin, H.M.A.; Mostafa, E.; Abd-El-Latif, A.A.; Iqbal, S.; Baltruschat, H. Electrodeposited Cobalt Nanosheets on Smooth Silver as a Bifunctional Catalyst for OER and ORR: In Situ Structural and Catalytic Characterization. *ACS Appl. Mater. Interfaces* **2022**, *14*, 55458–55470. [CrossRef]
46. Dai, J.; Zhu, Y.; Tahini, H.A.; Lin, Q.; Chen, Y.; Guan, D.; Zhou, C.; Hu, Z.; Lin, H.-J.; Chan, T.-S.; et al. Single-phase perovskite oxide with super-exchange induced atomic-scale synergistic active centers enables ultrafast hydrogen evolution. *Nat. Commun.* **2020**, *11*, 5657. [CrossRef]
47. Du, J.; Zhang, T.; Xing, J.; Xu, C. Hierarchical porous Fe_3O_4/Co_3S_4 nanosheets as an efficient electrocatalyst for the oxygen evolution reaction. *J. Mater. Chem. A* **2017**, *5*, 9210–9216. [CrossRef]
48. Hu, Y.; Zheng, Y.; Jin, J.; Wang, Y.; Peng, Y.; Yin, J.; Shen, W.; Hou, Y.; Zhu, L.; An, L.; et al. Understanding the sulphur-oxygen exchange process of metal sulphides prior to oxygen evolution reaction. *Nat. Commun.* **2023**, *14*, 1949. [CrossRef]
49. He, R.; Huang, X.; Feng, L. Recent Progress in Transition-Metal Sulfide Catalyst Regulation for Improved Oxygen Evolution Reaction. *Energy Fuels* **2022**, *36*, 6675–6694. [CrossRef]
50. Shi, J.; Jiang, H.; Hong, X.; Tang, J. Non-noble metal high entropy sulfides for efficient oxygen evolution reaction catalysis. *Appl. Surf. Sci.* **2024**, *642*, 158598. [CrossRef]

51. Kim, J.S.; Kim, B.; Kim, H.; Kang, K. Recent Progress on Multimetal Oxide Catalysts for the Oxygen Evolution Reaction. *Adv. Energy Mater.* **2018**, *8*, 1702774. [CrossRef]
52. Ahmed, A.T.A.; Sekar, S.; Khadtare, S.S.; Rochman, N.T.; Chinna, B.; Ansari, A.S. Anion-exchange synthesis of an $MnCo_2S_4$ electrocatalyst towards facilitated ultralong hydrogen evolution reaction in acidic and alkaline media. *CrystEngComm* **2024**, *26*, 215–222. [CrossRef]
53. Song, H.; Li, T.; He, T.; Wang, Z.; Fang, D.; Wang, Y.; Li, X.L.; Zhang, D.; Hu, J.; Huang, S. Cooperative catalytic Mo-S-Co heterojunctions with sulfur vacancies for kinetically boosted lithium-sulfur battery. *Chem. Eng. J.* **2022**, *450*, 138115. [CrossRef]
54. Kreider, M.E.; Burke Stevens, M. Material Changes in Electrocatalysis: An In Situ/Operando Focus on the Dynamics of Cobalt-Based Oxygen Reduction and Evolution Catalysts. *ChemElectroChem* **2023**, *10*, e202200958. [CrossRef]
55. Zou, X.; Liu, Y.; Li, G.-D.; Wu, Y.; Liu, D.-P.; Li, W.; Li, H.-W.; Wang, D.; Zhang, Y.; Zou, X. Ultrafast Formation of Amorphous Bimetallic Hydroxide Films on 3D Conductive Sulfide Nanoarrays for Large-Current-Density Oxygen Evolution Electrocatalysis. *Adv. Mater.* **2017**, *29*, 1700404. [CrossRef]
56. Hoang, T.T.H.; Gewirth, A.A. High Activity Oxygen Evolution Reaction Catalysts from Additive-Controlled Electrodeposited Ni and NiFe Films. *ACS Catal.* **2016**, *6*, 1159–1164. [CrossRef]
57. Peugeot, A.; Creissen, C.E.; Karapinar, D.; Tran, H.N.; Schreiber, M.; Fontecave, M. Benchmarking of oxygen evolution catalysts on porous nickel supports. *Joule* **2021**, *5*, 1281–1300. [CrossRef]
58. Cheng, X.; Lei, C.; Yang, J.; Yang, B.; Li, Z.; Lu, J.; Zhang, X.; Lei, L.; Hou, Y.; Ostrikov, K. Efficient Electrocatalytic Oxygen Evolution at Extremely High Current Density over 3D Ultrasmall Zero-Valent Iron-Coupled Nickel Sulfide Nanosheets. *ChemElectroChem* **2018**, *5*, 3866–3872. [CrossRef]
59. Meena, A.; Aqueel, A.A.T.; Narayan, S.A.; Gopalan, S.V.; Im, H.; Cho, S. Highly Efficient CoFeP Nanoparticle Catalysts for Superior Oxygen Evolution Reaction Performance. *Nanomaterials* **2024**, *14*, 1384. [CrossRef]
60. Lu, X.; Zhao, C. Electrodeposition of hierarchically structured three-dimensional nickel–iron electrodes for efficient oxygen evolution at high current densities. *Nat. Commun.* **2015**, *6*, 6616. [CrossRef]
61. Ahmed, A.T.A.; Lee, C.H.; Ansari, A.S.; Pawar, S.M.; Han, J.; Park, S.; Shin, G.; Yeon, S.; Cho, S.; Seol, J.; et al. Hybridized heterostructure of CoS and MoS_2 nanoparticles for highly-efficient and robust bifunctional water electrolysis. *Appl. Surf. Sci.* **2022**, *592*, 153196. [CrossRef]
62. Guo, D.; Qi, J.; Zhang, W.; Cao, R. Surface Electrochemical Modification of a Nickel Substrate to Prepare a NiFe-based Electrode for Water Oxidation. *ChemSusChem* **2017**, *10*, 394–400. [CrossRef] [PubMed]